Calculation of tunnel couplings in open gate-defined disordered quantum dot systems

Jan Klos,[*] Fabian Hassler, Pascal Cerfontaine, Hendrik Bluhm, and Lars R. Schreiber
JARA-FIT Institute for Quantum Information, Forschungszentrum Jülich GmbH and RWTH Aachen University, D-52074 Aachen, Germany

(Received 9 May 2018; published 26 October 2018)

Quantum computation based on semiconductor electron-spin qubits requires high control of tunnel couplings between the quantum dots and the electron reservoirs. Potential disorder and the increasing complexity of the two-dimensional gate-defined quantum computing devices set high demands on the gate design and the voltage tuning of the tunnel barriers. We present a Green's formalism approach for the calculation of tunnel couplings between a quantum dot and a reservoir. Our method takes into account in full detail the two-dimensional electrostatic potential of the quantum dot, the tunnel barrier, and the reservoir. A wideband limit is employed only far away from the tunnel barrier region where the density of states is sufficiently large. We calculate the tunnel coupling including potential disorder effects, which become increasingly important for large-scale silicon-based spin-qubit devices. Studying the tunnel couplings of a single-electron transistor in Si/SiGe as a showcase, we find that charged defects are the dominant source of disorder leading to variations in the tunnel coupling of four orders of magnitude.

DOI: 10.1103/PhysRevB.98.155320

I. INTRODUCTION

Gate-defined quantum dots (QDs) have proved to be a versatile platform for confining charge, electron-spin, and hole-spin quantum bits (qubits) in various material systems. Tremendous progress has been achieved in planar AlGaAs [1–6] and Si-based systems [7] such as complementary metal-oxide semiconductor structures [8,9], SiGe [10–13], and Si nanowires [14–17]. Focusing on scalability towards large-scale quantum systems [18–20], the complexity of the gate design increases, trending to denser gate configurations of QDs [10,11,21–24]. For scaling towards large numbers of qubits, it is essential to design the electrostatic gate patterns such that key parameters are nearly equal for each qubit, despite the typical electrostatic disorder present, due to imperfections of the host crystal lattice. Examples of such parameters are the inter-QD tunnel coupling and QD-to-reservoir tunnel coupling. Specifically, the tunnel coupling from the QD to electron reservoir has to be well controlled for spin-to-charge conversion schemes involving spin-state-dependent tunneling [1,25]. Charge readout of multiple QDs in close proximity has been demonstrated using single-electron transistors (SETs), for which tunnel barriers to both source and drain reservoirs have to be properly set [26].

Tunnel couplings can be tuned by gate voltages over a wide range [27,28]. Automatic tuning of a large number of quantum dots [29] would require, however, that the tunnel couplings be calculated for disorder potentials. Optimizing the gate design in this respect requires taking the details of the potential in the vicinity of the tunnel barriers into account. The increasing complexity of large-scale devices makes gate design development based on iterative fabrication and experimental studies alone very inefficient. Specific properties such as electrostatic disorder can be simulated prior to sample fabrication [30]. The tunnel coupling between two QDs (closed system) can be numerically calculated by solving the Schrödinger equation. Calculating the tunnel coupling between a QD and a reservoir (here defined as an open system) solving the full system is challenging. Several different approaches to take the tunnel coupling between a QD and a reservoir or between two reservoirs into account have been used, e.g., based on the master equation [31] or a transfer Hamiltonian [32–34], as well as self-consistent calculation schemes [35]. The Wentzel-Kramers-Brillouin (WKB) approximation, which is based on a semiclassical, one-dimensional trajectory of an electron [36–38], is prominent.

In this work, we present an approach for calculating the tunnel coupling in an open two-dimensional system based on Green's formalism with a wideband limit. Applying the wideband limit only far away from the tunnel barrier, this approach allows us to capture potential details of the reservoir region in close proximity to the QD. The calculation of the tunnel coupling is exact in principle and can be adapted to available computational resources by setting a boundary within the two-dimensional reservoir. The boundary divides the potential region which is fully quantum mechanically captured from the shapeless wideband approximated region. We validated our method on a two-dimensional model system with N sites and found the analytically calculated value for the tunnel coupling within a 6% error. The remaining small discrepancy is a result of our tight-binding model. The resulting error in the tunnel coupling could be easily compensated by tuning gate voltages during an experiment. We apply our method of calculating the tunnel couplings to an SET in a Si/SiGe heterostructure as a showcase. Since our method captures the full details of the electrostatic potential, we are able to study the effect of three different types of electrostatic disorder sources considered

[*]jan.klos@rwth-aachen.de

 ©2018 American Physical Society

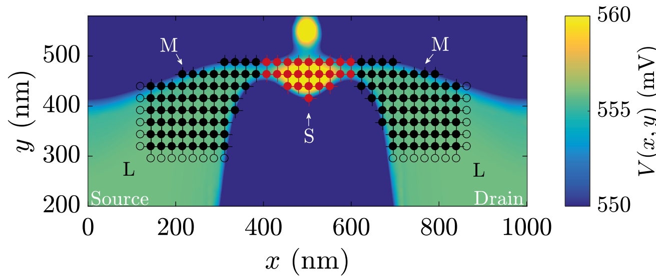

FIG. 1. Electrostatic potential of the SET overlaid by a 2D tight-binding model using nearest-neighbor coupling coupled to a quantum dot in a Si/SiGe heterostructure. The whole system (readout QD and reservoir) is divided into three subsystems containing the readout QD (system S, depicted in red), the electronic reservoir far away from the readout QD (system L, depicted by black circles), and an intermediate system (system M, depicted by black dots) connecting S and L. Using the wideband limit, only the first sites of system L have to be used. For the calculations, we consider a much higher density of sites (dots) than plotted here.

to be present in Si/SiGe heterostructures. For our SET gate design, we find that charged defects at the heterostructure surface are dominant and can lead to variation in the tunnel coupling of four orders of magnitude.

This paper is structured as follows: In Sec. II, we present the method for the calculation of tunnel couplings in open quantum systems based on Green's formalism. In Sec. III, we use the presented method on the electrostatic potential landscapes of our SET gate design, including three different disorder effects present in a Si/SiGe heterostructure as a showcase. In Appendix A, our numerical method is applied to an analytic two-dimensional (2D) toy-model system as a benchmark test, revealing a 6% error.

II. THEORY

To calculate the tunnel coupling t_C between a QD and its reservoirs, we take the following approach. We divide the whole system (dot and reservoir) into three adjacent, nonoverlapping subsystems: system S, which represents the QD; system L, which represents the electronic reservoir far away from the QD; and system M, which is an intermediate region connecting S and L (see Fig. 1). Each subsystem is tunnel coupled to the neighboring one. We are interested in the level broadening of the eigenstates of S due to the coupling to $M+L$. In a tunnel-Hamiltonian description in which system S is directly coupled to the reservoir, this level broadening is directly related to the tunnel-coupling matrix element t_C between the QD and reservoir. We will treat system L in the wideband limit (also called Markov approximation), meaning that we assume an energy-independent constant density of states ρ_L. Physically, this corresponds to assuming that system L is not affected by the system $S+M$ and that all electrons injected into L cannot return to the system. For the calculation of t_C, we follow a Green's formalism approach analogous to that in Ref. [39]. For the lead system with Hamiltonian H_L, the Green's function operator is defined by

$$\hat{G}_L(\hbar\omega) = \frac{1}{\hbar\omega - H_L}, \tag{1}$$

where $\hbar\omega$ is the energy parameter and $\hbar$ is the reduced Planck constant. Using the Kramers-Kronig relation, the Green's function is derived using the corresponding density of states ρ_L of the leads with

$$\hat{G}_L(\hbar\omega) = \int \frac{d\omega'}{2\pi\hbar} \frac{\rho_L(\omega')}{\omega - \omega' + i\eta^+}, \tag{2}$$

where η^+ is a positive regularization factor. Since the actual density of states of the reservoir is unknown, we assume a wideband limit (also called Markov approximation) with constant $\rho_L(\hbar\omega)$ [40,41]. Hence, Eq. (2) simplifies to

$$\hat{G}_L(\hbar\omega) = -i\pi\rho_L. \tag{3}$$

Alternatively, the Green's formalism is capable of describing the reservoir system analytically by infinite 2D plane waves. This leads to additional challenges, e.g., choosing a suitable 2D representations of plane waves, which are out of the scope of this work. Focusing on subsystem M coupled to the lead system and integrating out the lead, the effective nonhermitian Hamiltonian of the reservoir is

$$H_{M,\text{eff}} = H_M + w_{ML}^\dagger \hat{G}_L w_{ML}, \tag{4}$$

with the Hamiltonian H_M of the isolated intermediate system and w_{ML} being the coupling matrix between M and L. $H_{M,\text{eff}}$ is diagonalized with the eigenvalues $\epsilon_m - i\gamma_m$, with $\gamma_m > 0$, and left eigenvectors $\langle\Psi_{m'}|$ and right eigenvectors $|\Psi_m\rangle$. Note that $\langle\Psi_{m'}| \neq |\Psi_m\rangle^\dagger$ since $H_{M,\text{eff}}$ is non-Hermitian but both eigenvectors fulfill the biorthogonality relation

$$\langle\Psi_{m'}|\Psi_m\rangle = \delta_{m'm}. \tag{5}$$

With this procedure, we find the Green's function operator of subsystem M to be

$$\hat{G}_M(\hbar\omega) = \frac{1}{\hbar\omega - H_{M,\text{eff}}} = \sum_m \frac{|\Psi_m\rangle\langle\Psi_m|}{\hbar\omega - \epsilon_m + i\gamma_m + i\gamma_{\text{ext}}}, \tag{6}$$

where we introduce γ_{ext} as an additional external regularization parameter which compensates for the finite number of sites numerically taken into account. In Appendix A, we discuss the optimization of γ_{ext} in detail.

Focusing on subsystem S, the Hamiltonian H_S is solved by $H_S|s\rangle = \epsilon_s|s\rangle$ with the eigenvector $|s\rangle$ and its corresponding eigenvalue ϵ_s. The time evolution of a state $|s\rangle$ is described by its retarded Green's function

$$G_S(t) = -i\Theta(t)\langle s|e^{-iH_{\text{tot}}t}|s\rangle, \tag{7}$$

with H_{tot} being the Hamiltonian of the total system in S, where subsystems S and M are coupled by the matrix w_{SM} analogous to Eq. (4). The Fourier transform of Eq. (7) is

$$G_S(\hbar\omega) = \frac{1}{\hbar\omega - \epsilon_s - \Sigma_S(\hbar\omega)}, \tag{8}$$

where

$$\Sigma_S(\hbar\omega) = \langle s|w_{SM}^\dagger \hat{G}_M(\hbar\omega) w_{SM}|s\rangle \tag{9}$$

is the self-energy. The real part of Σ_S corresponds to an energetic shift within system S induced by the coupled system M, also called the Lamb shift [42]. This Lamb shift depends on all states within system M. In the following, we assume weak coupling between subsystem S and $M+L$. This corresponds to the physical situation where $|s\rangle$ is a well-defined state within S. The imaginary part of the

self-energy Σ_S leads to an energy-level broadening in system S, resembling a decay of the wave function $|s\rangle$. This decay corresponds to an electron within the QD which tunnels via the intermediate system M into the lead system. In this model, the energy-level broadening in S corresponds to the tunnel coupling of the state $|s\rangle$ given by

$$t_C = 2\,\mathrm{Im}[\Sigma_S(\epsilon_s)], \tag{10}$$

where the factor of 2 accounts for the decay of the probability instead of the probability amplitude as $|\Psi|^2 \propto \exp[-2\mathrm{Im}(\Sigma_S)t/\hbar] = \exp(-t_C t/\hbar)$.

Implementation recipe

For reference, we want to highlight all necessary steps to use the presented method for the calculation of tunnel couplings. We start with a computed electrostatic potential containing QDs and electron reservoirs. The Thomas-Fermi approximation is used to describe electron reservoirs, which imply significant screening effects. Regions containing a QD are calculated using superposition of the induced electrostatic potential of the modeled gate design which effectively neglects Coulomb interaction within the QD. For a subsequent transport calculation including more electrons in the QD, Coulomb interaction has to be taken into account. This electrostatic potential is then transferred to our tight-binding (TB) model with lattice spacing a. In this TB model, the tunnel coupling is calculated by following a three-step protocol: (i) We define the presented subsystems S and M. The truncation between S and M is defined perpendicular to the tunneling direction along the potential maximum of the tunnel barrier. At the maximum of the tunnel barrier the influence of the boundary conditions used is minimal for both subsystems. Subsystem L is defined as the remaining part of the reservoir, which is not covered by M and can be chosen by balancing out the importance of details of the reservoir potential versus computations power. (ii) We define the corresponding Hamiltonians H_S and H_M and coupling matrices w_{SM} and w_{ML}. Using Eq. (3) with a constant 2D density of states and w_{ML} in Eq. (4), $H_{M,\mathrm{eff}}$ is defined. (iii) By solving the eigenvalue problem of H_S and $H_{M,\mathrm{eff}}$, the self-energy Σ_S can be calculated using Eqs. (6) and (9). By solving the eigenvalue problem of H_S and inverting $G_M(\hbar\omega)$, Σ_S can be calculated directly. Finally, the tunnel coupling t_C is calculated using Eq. (10). Alternatively, t_C can also be calculated by using a computationally cheaper matrix inversion.

III. TUNNEL COUPLING IN REALISTIC SYSTEMS

In this section, we use the presented algorithm to calculate tunnel couplings of an open system including potential disorder with three different length scales λ in undoped Si/SiGe quantum wells. As a showcase, the electrostatic potential $V(x, y)$ of a QD capacitively coupled to a readout QD of an SET is used and shown in Fig. 2(a), computed solving the three-dimensional Poisson equation using the COMSOL MULTIPHYSICS software package [43]. In regions of high electron concentrations, e.g., reservoirs, screening effects lead to flat electrostatic potentials. Here, the Thomas-Fermi approximation is used. The shape of these reservoirs is defined by potential barriers exceeding the Fermi energy μ_F. The resulting computed electron density is shown in Fig. 2(b). In regions of expected low electron concentrations, e.g., QDs and tunnel barriers, the electrostatic potential is calculated using a linear superposition of the electrostatic potential of every gate independently. Within this section the Fermi energy is defined by $\mu_F = E_G/2 = 555$ meV, with an energy band gap of silicon $E_G = 1.11$ eV as a reference level. Since different reference levels require only a suitable set of gate voltages to induce a similar electrostatic potential, we want to point out that the cryogenic energy band gap of silicon is $E_G = 1.17$ eV for temperatures $T < 10$ K for completeness [44]. We define our tight-binding system using nearest-neighbor coupling with a spatial resolution $a = 1$ nm. The on-site potential V_{ij} is given by the previously computed electrostatic potential $V(x_i, y_j)$ at position $x_i = x/a$ and $y_i = y/a$. The nearest-neighbor coupling element is defined by $t_{ij} = \hbar^2\Delta_{ij}/2m^*a^2$, with m^* being the effective mass of electrons and Δ_{ij} being the discrete two-dimensional Laplacian [39]. By defining the separate subsystems according to the electrostatic confinement, we apply the presented method and calculate the tunnel coupling. To visualize the tunnel barrier in energetic height and width in one dimension, we calculate a semiclassical tunneling path $l(x, y)$ of an electron. To calculate $l(x, y)$, we use the Dijkstra algorithm [45] with on-site weights $\sqrt{2m^*a^2(V_{ij} - \epsilon_S)/\hbar^2}$. These weights are motivated by the one-dimensional WKB approximation. Along this path the potential is evaluated, and the tunnel barrier is characterized. This is shown in Fig. 2(a) and for the discussed types of disorder in Fig. 2(e). Note that $l(x, y)$ is sensitive to numerical errors and is not used to calculate t_C using our ansatz. For the potential landscape of the SET without any disorder effect included, the tunnel coupling of the readout QD with $\epsilon_S = E_G/2$ to the source reservoir is $t_L^{(\mathrm{ref})} = 1.3$ μeV. We obtained this result by using $\gamma_{\mathrm{ext}} = 700$ μeV in Eq. (6) and $N = 36\,589$ sites. We computed $n = 148$ eigenstates of system $M + L$ with energies in the vicinity of ϵ_S and found quality indicators $f_\gamma = 0.008$ and $f_n = 21.16$. The determination of n and the definition of the quality indicators are the subject of the Appendixes A and B. The tunnel coupling to the drain reservoir is $t_R^{(\mathrm{ref})} = 2.0$ μeV with $\gamma_{\mathrm{ext}} = 700$ μeV and $N = 36\,944$. We computed $n = 148$ eigenstates with $f_\gamma = 0.02$ and $f_n = 19.19$. For deviations from the tunnel barrier potential maximum between S and M on the scale of the used spatial resolution a, we calculate an error of tunnel coupling $\Delta t_L^{(\mathrm{ref})} = 0.3$ μeV and $\Delta t_R^{(\mathrm{ref})} = 0.4$ μeV. This error can be reduced by decreasing the lattice spacing of our tight-binding model. The tunnel couplings $t_L^{(\mathrm{ref})}$ and $t_R^{(\mathrm{ref})}$ are used as reference values for the effect of different disorder types on tunnel couplings.

A. Ge–Ge bond disorder

In SiGe unit cells, the specific arrangement of Si and Ge atoms in the diamond lattice leads to energy variations of the conduction band edge. From tight-binding simulations of periodic SiGe unit cells, Ge atoms on neighboring sites decrease the conduction band by approximately $\delta V = 100$ meV compared to a fully random barrier [46] and hence increase the energy of the electrons locally on the spatial resolution of an eight-atom unit cell. To model

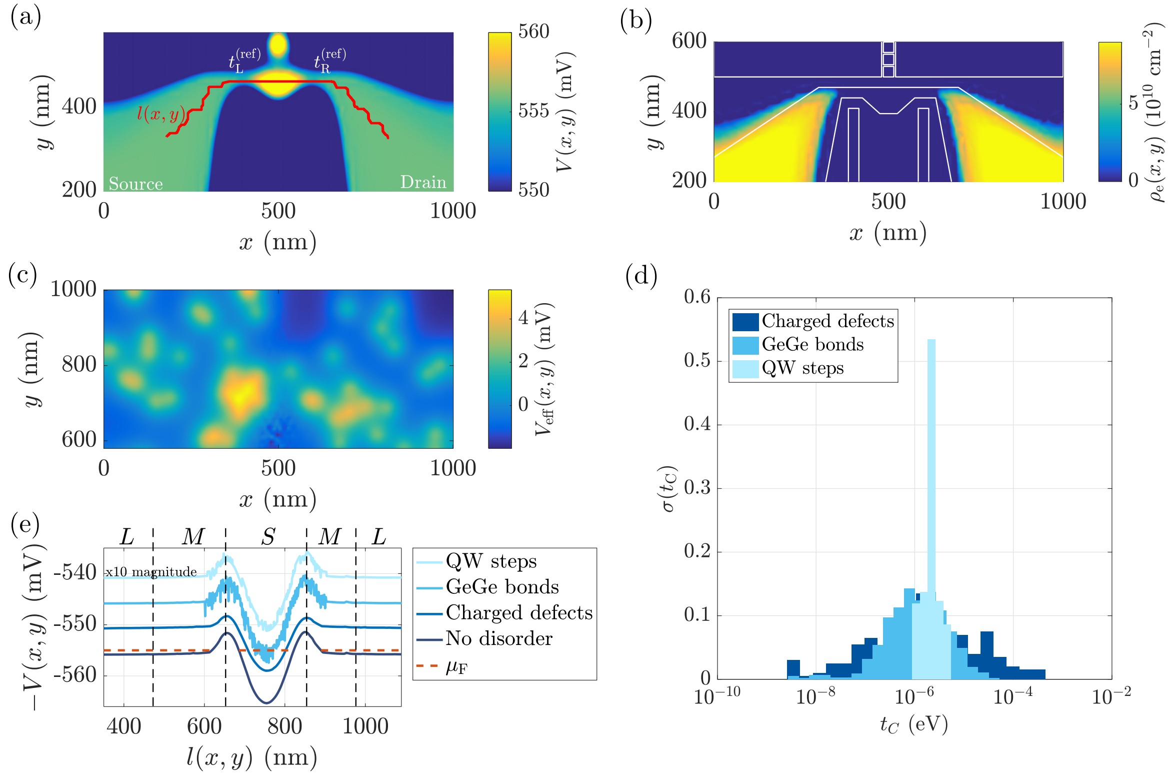

FIG. 2. (a) Tuned electrostatic potential $V(x, y)$ forming two reservoirs (source and drain), one readout QD, and an adjacent QD within the 2DEG layer in a Si/SiGe heterostructure. A qualitative semiclassical tunnel path of an electron from source to drain is shown by $l(x, y)$. (b) Electron density corresponding to (a) overlaid with the used gate structure (outlined by white lines). The Thomas-Fermi approximation is used in regions of high electron density to include screening effects leading to a flat potential. (c) Exemplary effective electrostatic potential induced by remote impurities located at the interface between the heterostructure and an oxide layer with a distance of 34 nm to the QW and a positive charge $q_e = e$, with e being the electron charge. (d) Normalized distribution of the simulated tunnel couplings $\sigma(t_C)$ for different types of disorder. QW steps as a possible source of disorder exhibit variations within one order of magnitude in t_C with $N_{dis} = 10^4$ random disorder configurations. Ge–Ge bonds as a possible source of disorder exhibit variations in two orders of magnitude around the reference value. Charged defects lead to variations in t_C of more than four orders of magnitude, $N_{dis} = 200$. The tunnel couplings without any disorder are $t_L^{(ref)} = 1.3\ \mu$eV and $t_R^{(ref)} = 2.0\ \mu$eV. (e) The electrostatic potential evaluated along the semiclassical tunnel path $l(x, y)$ for three different types of disorder in comparison to the case with no disorder. Within the reservoir where the Thomas-Fermi approximation is used, the effects of the disorder are screened by electrons. Potentials are offset by 5 mV for clarity. The potential fluctuations due to QW steps have to be enlarged by a factor of 10 prior to adding them to the gate-induced potential because otherwise they are not visible in the plot.

this disorder effect, we assume a binomial distribution $p_n(x)$ to find n Ge–Ge bonds surrounding a Ge-occupied site given an alloy composition factor x. To weight the disorder effect with respect to the electron envelope wave function $\Psi(z)$, the wave function overlap $F = \int_{z_I}^{\infty} |\Psi(z)|^2 dz$ with the SiGe layer ($z > z_I$) is included, where z_I is defined at the Si/SiGe interface. The resulting distribution $\chi_{\text{Ge–Ge}}$ and magnitude $m_{\text{Ge–Ge}}$ of potential variations ΔV over the number of Ge–Ge bonds n surrounding a single atom are

$$\chi_{\text{Ge–Ge}}(\Delta V) = p_n(x) x^n (1-x)^{4-n},$$
$$m_{\text{Ge–Ge}}(\Delta V) = -\frac{n}{2}\delta V F. \tag{11}$$

The factor of 1/2 in magn(ΔV) accounts for the double counting of each bond when iterating over the eight-atom unit cell. Finally, we define the length scale of this fluctuation by the lattice constant of the $\text{Si}_{(1-x)}\text{Ge}_x$ alloy with $\lambda_{\text{Ge–Ge bonds}} \approx 0.5$ nm and transfer the presented potential variations to our tight-binding model. The model results in a number of Ge–Ge bonds $n = 6 \pm 4/\text{nm}^{-2}$, where we neglect further variations along z. The nonzero average of the Ge–Ge bonds leads to an average increase in the electron energy of $\Delta\bar{V} = 2.5$ meV. This energy offset is neglected within the following study since it is compensated by an initial tuning of the electrostatic potential. By adding ΔV to the electrostatic potential, the tunnel coupling can be calculated as before. The resulting effect on the electrostatic potential is shown by the semiclassical tunnel path in Fig. 2(e). The normalized distribution $\sigma(t_C)$ of the calculated tunnel coupling t_C for $N_{dis} = 10^4$ randomly generated Ge–Ge bond ensembles is shown in Fig. 2(d). Due to the small length scale $\lambda_{\text{Ge–Ge bonds}}$ and the comparable magnitude of the variation with respect to the barrier height, this modeled disorder leads to varying tunnel couplings within two orders of magnitude compared to the reference value.

B. Quantum well step disorder

Interface roughness has been reported to be a major source of disorder leading to variations of the valley splitting [47]. Furthermore, atomic steps at the interface of Si/SiGe result

in changes in the confinement along the growth direction and hence to a fluctuation in the energy of the electrons. To model the latter effect, we restrict ourselves to relative changes of only one step at each interface. Assuming effective single-layer growth using molecular beam epitaxy, the step height is $h_{\mathrm{Step}} = a_{\mathrm{SiGe}}/4 = 0.135$ nm. This leads to three different confinement energies, E_0, E_+, and E_-, along z. E_0 is the energy for a quantum well (QW) without any additional step. E_+ is the energy for a QW with a width decreased by one interface step h_{Step}, and E_- is the energy for a QW with a width increased by h_{Step}. The resulting potential variation is

$$\Delta V_\pm = -(E_0 - E_\pm), \tag{12}$$

where E_0 and $E_\pm$ are the energies of the three different confinements as defined above. These energies are calculated for an applied voltage bias of E_G/e, a QW width of 12 nm, and a conduction band minimum difference of $\Delta E_c = 160$ meV of the heterostructure. There is no potential offset $\Delta\bar{V}_\pm = 0$ by construction. Furthermore, we define the length scale of this fluctuation to vary uniformly in the range of $\lambda_{\mathrm{QDstep}} =$ 1–24 nm, corresponding to wafer miscut angles of $\alpha =$ 7.8°–0.3°. The tunnel coupling is calculated as before. The effect of this type of disorder on the semiclassical tunnel path is shown in Fig. 2(e), where due to the small magnitude of approximately 100 μeV, the potential fluctuations are multiplied by a factor of 10. Due to the relatively long coherence length $\lambda_{\mathrm{QWstep}}$ and the small magnitude of the variation compared to the tunnel barrier height, this disorder effect leads to variation in the tunnel couplings smaller than one order of magnitude compared to the reference value, as shown in Fig. 2(d). Note that we did not include phase shifts of valley states generated by the SiGe interface roughness [48]. Arguably, the valley tunnel blockade known from double quantum dots plays a minor role for the tunnel coupling of a quantum dot to a reservoir, as the density of states of the latter is continuous. Valley effects will be investigated in more detail in future work.

C. Impurities

We refer to positively charged defects located in the heterostructure as impurities. Depending on the location, charged defects can have a significant influence on the tunnel barrier [49]. Impurities formed by oxygen atoms located near and within the Si QW have been reported with concentrations of 10^{10}–10^{11} cm^{-2} introduced during the growth of the heterostructure in a chemical vapor deposition reactor [50]. Remote impurities located at the interface between the heterostructure and an Al_2O_3 oxide layer have been suggested to dominate electron scattering [51]. In this section, we introduce impurities located at the interface of the heterostructure and a possible oxide layer 34 nm above the QW. All impurities are positively charged with $q_{\mathrm{Imp}} = e$, with e being the elementary electric charge, and randomly distributed over the interface, leading to a concentration of 10^{10} cm^{-2}. By adding these impurities directly within our COMSOL model, the dielectric properties of the modeled heterostructure including the gate design are incorporated. In comparison to the initially tuned potential without disorder, these impurities lead to a resulting average positive offset $\bar{V}_{\mathrm{Imp}} \approx 3.5$ mV, with a standard deviation of the potential fluctuations of $\Delta V_{\mathrm{Imp}} \approx 1.3$ mV, as shown in Fig. 2(c). We compensate $\bar{V}_{\mathrm{Imp}}$ by a global voltage offset of $V_{\mathrm{comp}} = \bar{V}_{\mathrm{Imp}}$ applied to all gates used for each single-impurity ensemble. This is a rather simple compensation scheme which requires only a global voltage parameter to be set. In this manner, we compensate the potential and end up with two tunnel barriers with a probability of 59% and at least one tunnel barrier with a probability of 96% using 100 randomly chosen impurity ensembles. Within an experiment, the global voltage can be tuned more precisely to achieve the desired tunnel couplings. By calculating the tunnel coupling from the source reservoir into the readout QD (left barrier) and the readout QD into the drain reservoir (right barrier), we quantify the effect of impurities on the functionality of our SET for several different impurity distributions. The resulting distribution of the tunnel couplings is shown in Fig. 2(d) and varies over four orders of magnitude using the simple compensation scheme. This type of disorder resembles the strongest variation in t_C compared to the previous discussed effects. We observe differences in the tunnel couplings between the left and right tunnel barriers up to several meV, as shown in Fig. 3. The different distributions of positively charged impurities are indexed by i and sorted with respect to the tunnel coupling of the left barrier. Ensembles with only one remaining tunnel barrier are included within this plot ($i \geqslant 91$) and show the largest disorder impact on the tunnel barriers. Here, the Fermi energy exceeds the height of the left tunnel barrier. Note that left and right tunnel barriers are uncorrelated in Fig. 3. Thus, a precisely tuned global voltage is insufficient to tune both tunnel couplings. It requires involved individual tuning of gate voltages to set both tunnel barriers as desired.

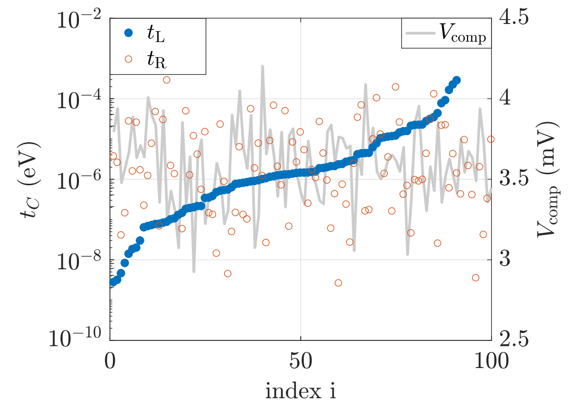

FIG. 3. Calculated tunnel coupling for $N_{\mathrm{dis}} = 100$ randomly distributed positively charged impurities with a concentration of 10^{10} cm^{-2}. The presented data are sorted with respect to t_L. For every impurity distribution i, the resulting tunnel couplings t_L and t_R and the corresponding global compensation voltage V_{comp} are shown.

IV. CONCLUSION

We presented a method for calculating tunnel couplings of open quantum systems. We aimed especially at the simulation of gate patterns and disorder for gated semiconductor quantum computers. We applied this method to a gate layout of an SET charge detector as a showcase. The method is applicable to various systems and is flexible with respect to available computational resources while including all

modeled details of the electrostatic potential. The wideband limit is solely used for the reservoir region far away from the barrier. Basic models for three different disorder sources, typical for Si/SiGe heterostructures, are used to study the effect of electrostatic disorder on the tunnel coupling of the SET, pointing towards charged defects as a strong source of varying tunnel coupling over four orders of magnitude. While a detailed model of disorder potential in Si/SiGe is beyond the scope of our work, we expect that our method can be used to calculate tunnel couplings with improved noise models of various material systems.

ACKNOWLEDGMENTS

We thank F. Haupt for proofreading the manuscript. P.C. acknowledges support from Deutsche Telekom Stiftung. This project is sponsored by the Federal Ministry of Education and Research under Contract No. FKZ: 13N14778. Project Si-QuBus has received funding from the QuantERA ERA-NET Cofund in Quantum Technologies implemented within the European Union's Horizon 2020 Programme.

APPENDIX A: VALIDATION

To test this approach, we apply the presented method to an analytically solvable tight-binding toy-model system. The validation focuses on the use of the presented wideband limit and on the calculated tunnel coupling. The toy-model system is two-dimensional and consists of a single site coupled by the transition element w to a 2D lattice with N sites. Within the 2D lattice, adjacent sites are coupled by nearest-neighbor transition elements t. To define the presented subsystems, the 2D toy model is schematically shown in Fig. 4(a). The single site is defined as subsystem S, depicted in blue. Subsystem M is defined by all inner sites of the 2D lattice and is depicted in red. Without further restriction subsystem S is coupled to the middle site of subsystem M. The outer sites of the 2D lattice are defined as subsystem L, depicted in yellow. Since we approximate the lead system, it is sufficient to account for only the sites, which are directly coupled to system M.

1. Wideband limit

First, we validate the wideband limit in the lead system. Therefore, we compare the computed numerical density of states of the 2D toy-model system using the wideband limit with the density of states for a discrete infinite 2D lattice. The latter is calculated analytically [52]:

$$\rho_{\mathrm{M,analytic}}(\hbar\omega) = \frac{1}{2t\pi^2} K\left[1 - \left(\frac{\hbar\omega - V_0 - 4t}{4t}\right)^2\right], \quad 0 < |\hbar\omega| \leqslant V_0 + 4t. \tag{A1}$$

Note that if the analytic expression of $\rho_{\mathrm{M,analytic}}$ were known for all problems, we could use $\rho_{\mathrm{M,analytic}}(\hbar\omega)$ in Eq. (2) and calculate $H_{\mathrm{M,eff}}$ using Eq. (4) and thus calculate t_{C} analytically. Since in most realistic problems $\rho_{\mathrm{M,analytic}}$ is unknown, we use Eq. (3), the wideband limit, instead of the Kramers-Kronig relation in Eq. (2). For a 2D toy model with $N = 1521$ sites and $t = 1$, the numerical and analytic densities of states are shown in Fig. 4(b). The numerical density of states of the 2D lattice can be calculated using Eq. (6) with $\rho_{\mathrm{M}}(\hbar\omega) = -i\mathrm{Tr}[\hat{G}_{\mathrm{M}}(\hbar\omega)]$ [39]. Up to a fluctuation of the numerical density of states, both solutions coincide and follow the same behavior with respect to the energy $\hbar\omega$. For $\hbar\omega \approx 0$, both solutions exhibit a Van Hove singularity [53]. In the vicinity of the energy band edge $|\hbar\omega| \approx 4t$, the deviation between the analytic and numerical solutions increases. This is explained by the decreasing imaginary part of the energy levels, leading to more δ-function-shaped states. For energies $0 < |\hbar\omega| < 4t$, the analytic density of states is rather constant. In comparison to the infinite system, the finite size of the model leads to an overall fluctuation. Focusing on states $|\Psi_m\rangle$ and calculating $\mathrm{Re}[\langle\Psi_m|\hat{G}_{\mathrm{M}}(\hbar\omega)|\Psi_m\rangle]$, all energy levels are approximately Cauchy-Lorentz shaped. Due to the nonequidistant energetic distribution of the energy levels, the energetic overlap of neighboring states varies, resulting in a nonconstant density of states [see the inset in Fig. 4(b)]. Hence, the fluctuation is a function of energy $\hbar\omega$ and system size N. For a finite number of sites N in the 2D toy model, this fluctuation can be compensated by an additional external decay parameter γ_{ext} used as regularization factor, which is added to $i\gamma_m \rightarrow i(\gamma_m + \gamma_{\mathrm{ext}})$, as already introduced in Eq. (6). To define a quality indicator for the fluctuation, we use

$$f_\gamma = \left.\frac{A_{\rho_{\mathrm{M}}}}{\rho_{\mathrm{M,max}}}\right|_{\hbar\omega=\epsilon_{\mathrm{S}}}, \tag{A2}$$

where $A_{\rho_{\mathrm{M}}}(\hbar\omega)$ is the maximum amplitude of the local fluctuation defined in the energetic range of multiple neighboring states and $\rho_{\mathrm{M,max}}$ is the maximal value of ρ_{M}, both of which are evaluated at the same energy $\hbar\omega$ [see the inset of Fig. 4(b)]. To compensate the fluctuation, we increase γ_{ext} until $\partial f_\rho/\partial\gamma_{\mathrm{ext}}$ saturates at a minimum. In this way, we determine the optimal value for γ_{ext}, labeled $\gamma_{\mathrm{ext,opt}}$. For the validation of the toy model and the numeric calculation of the tunnel couplings of the SET, we used $A_{\rho_{\mathrm{M}}}(\hbar\omega)$ in the energetic interval of five neighboring energy levels after subtracting the overall tendency of ρ_{M} approximated by a linear offset. Determining $\gamma_{\mathrm{ext,opt}}$ as described above, the numerical and analytic densities of states coincide very well for the energy used and a given number of sites N, as can be seen from Fig. 4(c) for $\hbar\omega = -2$ with all states N taken into account. Note that particularly for the model validation, f_γ does not include any information of the analytic solution.

2. Tunnel coupling

Now, we validate the calculation of the tunnel coupling t_{C} using the presented method on our 2D toy model. By using a constant on-site potential V_0 in system $M + L$, we calculate the analytic solution of the tunnel coupling for an arbitrary energy $\hbar\omega$ to be

$$t_{\mathrm{C,analytic}}(\hbar\omega) = 2\pi w^2 \rho_{\mathrm{M,analytic}}(\hbar\omega), \tag{A3}$$

with $w = 0.1$ ensuring weak coupling of S to $M + L$. In the following, we explicitly focus on a single energy level $|\mathrm{s}\rangle$ in subsystem S with energy ϵ_{S} and energy-conserving tunneling. The computed relative tunnel couplings $t_{\mathrm{C}}/t_{\mathrm{C,analytic}}$ are shown for the two dependencies $\hbar\omega = \epsilon_{\mathrm{s}}$ and N in Fig. 4(d). For every point, f_ρ is minimized by $\gamma_{\mathrm{ext,opt}}$. By varying ϵ_{s}, the numerical tunnel coupling differs from the analytic solution

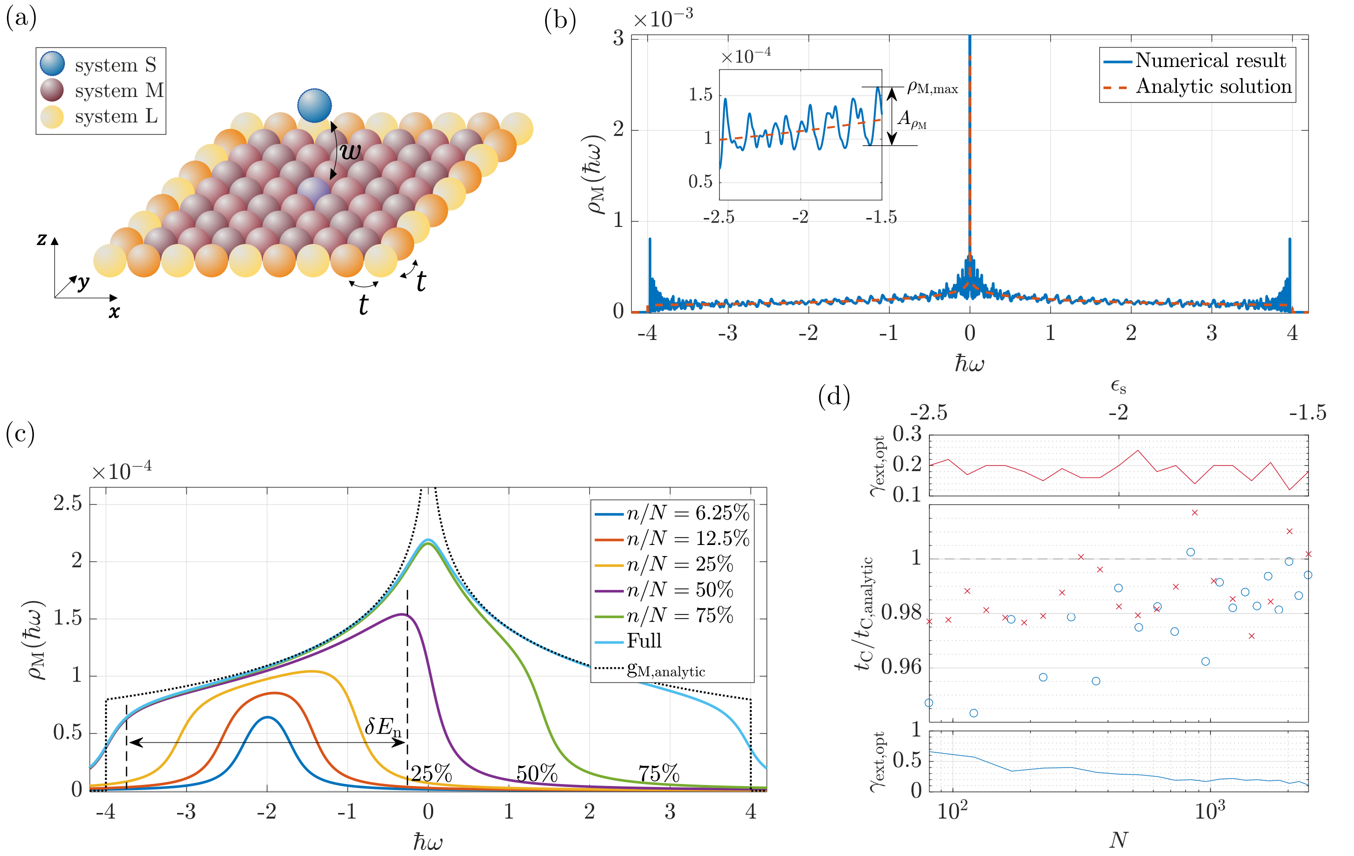

FIG. 4. (a) Schematic of the 2D tight-binding toy model with a single site coupled by the transition element w to a 2D lattice with N sites, each coupled by the nearest-neighbor transition element t. (b) Comparison of the density of states for an infinite 2D lattice: numerical solution using the wideband limit vs the analytic solution. For $\hbar\omega \approx 0$, both solutions diverge due to the Van Hove singularity. Close to the band edge with $|\hbar\omega| \approx 4t$, the deviation between the analytic and numerical solutions increases. In the numerical simulation, the 2D lattice consists of $N = 1521$ sites coupled by nearest-neighbor coupling with $t = 1$. (c) Density of states for a 2D lattice with $j_{\text{ext,opt}} = 0.2$ chosen with respect to $N = 1521$ and $\hbar\omega = \epsilon_S = -2$ for different calculated fractions n/N of the full solution of H_M. By reducing the fraction of computed states n/N, $\rho_{M,n<N}$ deviates from theory. (d) Dependency of the numerical tunnel coupling t_C and the optimal external decay $\gamma_{\text{ext,opt}}$ on system size N of the 2D lattice and energy level ϵ_S of the single site. The single site is coupled by the transition element $w = 0.1$. The 2D lattice is defined with $N = 1521$ and $t = 1$. Varying ϵ_S, the numerical tunnel couplings differ from the analytic solution up to an error of 3%, where $\gamma_{\text{ext,opt}}$ shows a constant tendency. Varying N, the numerical tunnel couplings differ from the analytic solution up to an error of 6%. The external decay $\gamma_{\text{ext,opt}}$ shows a decreasing tendency for increasing N.

with an error of up to 3% where $\gamma_{\text{ext,opt}}$ does not exhibit a clear tendency over $\hbar\omega = \epsilon_s$ and varies only due to the varying local fluctuation. For different system sizes N, the numerical tunnel coupling differs from the analytic solution by an error of up to 6% where $\gamma_{\text{ext,opt}}$ decreases for increasing system sizes N. Since in a tight-binding model with system size N, there are exactly N energy levels, the intrinsic energetic difference between neighboring states decreases with increasing system size, resulting in a decreasing $\gamma_{\text{ext,opt}}$. With system size $N > 10^3$, the error may be reduced even further but might lead to computational challenges.

APPENDIX B: TRANSFER TO LARGE SYSTEM SIZES

For large system sizes, e.g., in our realistic showcase with $N \approx 10^5$, solving the Schrödinger equation of the complete system may exceed available computational resources. Therefore, we discuss the influence of computing only n states around ϵ_S of the total N states in subsystem M. The numerical density of states for different fractions $0 < n/N \leqslant 1$ is shown in Fig. 4(c). For the full solution of the Schrödinger equation ($n = N$), the analytic and numerical densities of states coincide using $\gamma_{\text{ext,opt}} = 0.2$ for $\epsilon_S = -2$ and $N = 1521$. Due to the external decay, the Van Hove singularity at $\hbar\omega = 0$ is suppressed, and the band edges at $|\hbar\omega| = 4t$ are smeared out. Since the overlap of energetically far distant states is negligible, we compute only states within the energetic proximity of ϵ_s. This reduces the required computational resources drastically. For lower fractions (here $n/N < 50\%$), the numerical density of states deviates from the analytic solution since we neglect states which contribute to the density of states and tunnel coupling at the energy ϵ_s. Like for f_ρ, we define an additional quality indicator:

$$f_n = \frac{\delta E_n}{\gamma_m + \gamma_{\text{ext}}}, \tag{B1}$$

where we use the energetic interval δE_n which is spanned by these n computed states with respect to the broadening

$\gamma_m + \gamma_{ext}$ of the states in close energetic proximity to ϵ_s. This is shown for $n/N = 50\%$ in Fig. 4(c).

Within the validation, we explicitly focused on small system sizes ($N \approx 10^3$), leading especially to errors due to the finite size of the system. For larger system sizes with $N \gtrsim 10^5$ sites, this error is captured intrinsically, and small additional external decay γ_{ext} can be included to minimize f_ρ. On the other hand, the second indicator in Eq. (B1) leads to a tremendous reduction of computational resources dominated by the dimension of $H_{M,eff}$, while still ensuring reasonable results.

[1] R. Hanson, L. P. Kouwenhoven, J. R. Petta, S. Tarucha, and L. M. K. Vandersypen, Rev. Mod. Phys. **79**, 1217 (2007).

[2] K. C. Nowack, M. Shafiei, M. Laforest, G. E. D. K. Prawiroatmodjo, L. R. Schreiber, C. Reichl, W. Wegscheider, and L. M. K. Vandersypen, Science **333**, 1269 (2011).

[3] M. D. Shulman, O. E. Dial, S. P. Harvey, H. Bluhm, V. Umansky, and A. Yacoby, Science **336**, 202 (2012).

[4] J. Medford, J. Beil, J. M. Taylor, S. D. Bartlett, A. C. Doherty, E. I. Rashba, D. P. Divincenzo, H. Lu, A. C. Gossard, and C. M. Marcus, Nat. Nanotechnol. **8**, 654 (2013).

[5] J. Yoneda, T. Otsuka, T. Nakajima, T. Takakura, T. Obata, M. Pioro-Ladrière, H. Lu, C. J. Palmstrøm, A. C. Gossard, and S. Tarucha, Phys. Rev. Lett. **113**, 267601 (2014).

[6] T. Botzem, R. P. G. McNeil, J.-M. Mol, D. Schuh, D. Bougeard, and H. Bluhm, Nat. Commun. **7**, 11170 (2016).

[7] F. A. Zwanenburg, A. S. Dzurak, A. Morello, M. Y. Simmons, L. C. L. Hollenberg, G. Klimeck, S. Rogge, S. N. Coppersmith, and M. A. Eriksson, Rev. Mod. Phys. **85**, 961 (2013).

[8] M. Veldhorst, J. C. C. Hwang, C. H. Yang, A. W. Leenstra, B. de Ronde, J. P. Dehollain, J. T. Muhonen, F. E. Hudson, K. M. Itoh, A. Morello, and A. S. Dzurak, Nat. Nanotechnol. **9**, 981 (2014).

[9] M. Veldhorst, C. H. Yang, J. C. C. Hwang, W. Huang, J. P. Dehollain, J. T. Muhonen, S. Simmons, A. Laucht, F. E. Hudson, K. M. Itoh, A. Morello, and A. S. Dzurak, Nature (London) **526**, 410 (2015).

[10] M. G. Borselli, K. Eng, R. S. Ross, T. M. Hazard, K. S. Holabird, B. Huang, A. A. Kiselev, P. W. Deelman, L. D. Warren, I. Milosavljevic, A. E. Schmitz, M. Sokolich, M. F. Gyure, and A. T. Hunter, Nat. Nanotechnol. **26**, 375202 (2015).

[11] D. M. Zajac, T. M. Hazard, X. Mi, E. Nielsen, and J. R. Petta, Phys. Rev. Appl. **6**, 054013 (2016).

[12] T. F. Watson, S. G. J. Philips, E. Kawakami, D. R. Ward, P. Scarlino, M. Veldhorst, D. E. Savage, M. G. Lagally, M. Friesen, S. N. Coppersmith, M. A. Eriksson, and L. M. K. Vandersypen, Nature (London) **555**, 633 (2018).

[13] J. Yoneda, K. Takeda, T. Otsuka, T. Nakajima, M. R. Delbecq, G. Allison, T. Honda, T. Kodera, S. Oda, Y. Hoshi, N. Usami, K. M. Itoh, and S. Tarucha, Nat. Nanotechnol. **13**, 102 (2018).

[14] B. Voisin, V. H. Nguyen, J. Renard, X. Jehl, S. Barraud, F. Triozon, M. Vinet, I. Duchemin, Y. M. Niquet, S. De Franceschi, and M. Sanquer, Nano Lett. **14**, 2094 (2014).

[15] A. C. Betz, M. L. V. Tagliaferri, M. Vinet, M. Broström, M. Sanquer, A. J. Ferguson, and M. F. Gonzalez-Zalba, Appl. Phys. Lett. **108**, 203108 (2016).

[16] M. Brauns, J. Ridderbos, A. Li, W. G. van der Wiel, E. P. A. M. Bakkers, and F. A. Zwanenburg, Appl. Phys. Lett. **109**, 143113 (2016).

[17] R. Maurand, X. Jehl, D. Kotekar-Patil, A. Corna, H. Bohuslavskyi, R. Laviéville, L. Hutin, S. Barraud, M. Vinet, M. Sanquer, and S. De Franceschi, Nat. Commun. **7**, 13575 (2016).

[18] C. D. Hill, E. Peretz, S. J. Hile, M. G. House, M. Fuechsle, S. Rogge, M. Y. Simmons, and L. C. L. Hollenberg, Sci. Adv. **1**, e1500707 (2015).

[19] L. M. K. Vandersypen, H. Bluhm, J. S. Clarke, A. S. Dzurak, R. Ishihara, A. Morello, D. J. Reilly, L. R. Schreiber, and M. Veldhorst, NPJ Quantum Inf. **3**, 34 (2017).

[20] M. Veldhorst, H. G. J. Eenink, C. H. Yang, and A. S. Dzurak, Nat. Commun. **8**, 1766 (2017).

[21] M. R. Delbecq, T. Nakajima, T. Otsuka, S. Amaha, J. D. Watson, M. J. Manfra, and S. Tarucha, Appl. Phys. Lett. **104**, 183111 (2014).

[22] T. A. Baart, P. T. Eendebak, C. Reichl, W. Wegscheider, and L. M. K. Vandersypen, Appl. Phys. Lett. **108**, 213104 (2016).

[23] D. M. Zajac, T. M. Hazard, X. Mi, K. Wang, and J. R. Petta, Appl. Phys. Lett. **106**, 223507 (2015).

[24] H. Flentje, P.-A. Mortemousque, R. Thalineau, A. Ludwig, A. D. Wieck, C. Bäuerle, and T. Meunier, Nat. Commun. **8**, 501 (2017).

[25] J. M. Elzermann, R. Hanson, L. Wllems van Beveren, B. Witkamp, L. M. K. Vandersypen, and L. P. Kouwenhoven, Nature (London) **430**, 431 (2004).

[26] C. Barthel, D. J. Reilly, C. M. Marcus, M. P. Hanson, and A. C. Gossard, Phys. Rev. Lett. **103**, 160503 (2009).

[27] M. G. Borselli, K. Eng, E. T. Croke, B. M. Maune, B. Huang, R. S. Ross, A. A. Kiselev, P. W. Deelman, I. Alvarado-Rodriguez, A. E. Schmitz, M. Sokolich, K. S. Holabird, T. M. Hazard, M. F. Gyure, and A. T. Hunter, Appl. Phys. Lett. **99**, 063109 (2011).

[28] S. Rochette, M. Rudolph, A. M. Roy, M. Curry, G. T. Eyck, R. Manginell, J. Wendt, T. Pluym, S. M. Carr, D. Ward, M. P. Lilly, M. S. Carroll, and M. Pioro-Ladrière, arXiv:1707.03895.

[29] S. S. Kalantre, J. P. Zwolak, S. Ragole, X. Wu, N. M. Zimmerman, M. D. Stewart, and J. M. Taylor, arXiv:1712.04914 .

[30] A. Frees, J. K. Gamble, D. R. Ward, R. Blume-Kohout, M. A. Eriksson, M. Friesen, and S. N. Coppersmith, arXiv:1409.3846.

[31] R. Ziegler, C. Bruder, and H. Schoeller, Phys. Rev. B **62**, 1961 (2000).

[32] J. Bardeen, Phys. Rev. Lett. **6**, 57 (1961).

[33] C. Noguera, J. Phys. (Paris) **50**, 2587 (1989).

[34] M. Friesen, M. Y. Simmons, and M. A. Eriksson, arXiv:1310.6115.

[35] X. Gao, D. Mamaluy, E. Nielsen, R. W. Young, A. Shirkhorshidian, M. P. Lilly, N. C. Bishop, M. S. Carrol, and R. P. Muller, J. Appl. Phys. **115**, 133707 (2014).

[36] A. Garg, Am. J. Phys. **68**, 430 (2000).

[37] V. Jelic and F. Marsiglio, Eur. J. Phys. **33**, 1651 (2012).

[38] Z. Ahmed, Phys. Rev. A **47**, 4761 (1993).

[39] S. Datta, *Electronic Transport in Mesoscopic Systems*, Cambridge Studies in Semiconductor Physics and Microelectronic Engineering (Cambridge University Press, Cambridge, 1995).

[40] G. Stefanucci and R. van Leeuwen, *Nonequilibrium Many-Body Theory of Quantum Systems: A Modern Introduction* (Cambridge University Press, Cambridge, 2013).
[41] C. Cohen-Tannoudji, J. Dupont-roc, and G. Grynberg, *Atom-Photon Interactions: Basic Processes and Applications* (Wiley-VCH, Weinheim, 2004).
[42] W. E. Lamb and R. C. Retherford, Phys. Rev. **72**, 241 (1947).
[43] COMSOL MULTIPHYSICS, version 5.2, COMSOL AB, Stockholm, Sweden.
[44] W. Bludau, A. Onton, and W. Heinke, J. Appl. Phys. **45**, 1846 (1974).
[45] E. W. Dijkstra, Numerische Math. **1**, 269 (1959).
[46] Z. Jiang, N. Kharche, T. Boykin, and G. Klimeck, Appl. Phys. Lett. **100**, 103502 (2012).
[47] N. Kharche, M. Prada, T. B. Boykin, and G. Klimeck, Appl. Phys. Lett. **90**, 092109 (2007).
[48] M. Friesen and S. N. Coppersmith, Phys. Rev. B **81**, 115324 (2010).
[49] R. Rahman, E. Nielsen, R. P. Muller, and M. S. Carroll, Phys. Rev. B **85**, 125423 (2012).
[50] X. Mi, T. M. Hazard, C. Payette, K. Wang, D. M. Zajac, J. V. Cady, and J. R. Petta, Phys. Rev. B **92**, 035304 (2015).
[51] J.-Y. Li, C.-T. Huang, L. P. Rokhinson, and J. C. Sturm, Appl. Phys. Lett. **103**, 162105 (2013).
[52] R. Piasecki, arXiv:0804.1037.
[53] L. Van Hove, Phys. Rev. **89**, 1189 (1953).